Analysis and Design of Plasmonic-Organic Hybrid Electro-Optic Modulators Based on Directional Couplers

Alberto Tibaldi [iD], *Member, IEEE*, Mohammadamin Ghomashi, Francesco Bertazzi [iD], Marco Vallone [iD], Michele Goano [iD], *Senior Member, IEEE*, and Giovanni Ghione [iD], *Life Fellow, IEEE*

Abstract—We present a detailed simulation study on plasmonic-organic hybrid electro-optic modulators based on coupled symmetric or asymmetric plasmonic slots. An electro-optic polymer is exploited as an active material, and the device is compatible with a silicon photonics platform. The proposed device operates at 1550 nm wavelength, typical of data center or long-haul telecommunication systems. The device performance in terms of area, plasmonic losses, optical bandwidth, intrinsic modulation bandwidth and energy dissipation are comparable to already proposed Mach-Zehnder solutions, but with potentially better extinction ratio, coupling losses due to photonic-plasmonic transitions, and flexibility in exploiting, without any performance penalty, asymmetric slots to shift the ON and OFF states bias. Finally, the bias dependence of the modulation chirp is investigated, comparing through and cross-coupling configurations.

Index Terms—Electro-optical systems, optoelectronic materials.

I. INTRODUCTION

ELECTRO-OPTIC (EO) modulators play an important role in high-speed, high-capacity telecommunication systems. The two main implementations of EO modulators are the Mach-Zehnder (MZ) and the resonant ring modulator, see the recent review [1]; a third, somewhat less popular, implementation is the directional coupler (DC) modulator, already proposed in the 1970s [2]. High-speed EO modulators exploit a variety of EO materials operating on the basis of several fast physical effects, which imply a variation of the complex refractive index caused by the applied electric field. Examples are the Pockels/Kerr effects (perovskites, III-V semiconductors, and chromophore-loaded polymers) and the Franz-Keldysh and quantum confined Stark effects (III-V bulk or quantum-well semiconductor structures, respectively); the plasma effect, related to free carrier

injection, is instead exploited in Si and indium tin oxide (ITO) based devices [1].

Within this context, plasmonic-organic hybrid (POH) modulator approaches show an interesting potential for EO modulator integration in Si photonic platforms [3] due to their micron-scale size, small enough to facilitate co-integration with CMOS electronics [4], and exhibit record speed (already with a concentrated electrode setup) and potentially lower ON-OFF driving voltages than in silicon-organic hybrid (SOH) approaches [5]. Indeed, in POH modulators, plasmonic modes allow for strongly localized optical fields, with excellent overlap with the RF fields, much better than in their SOH counterparts [6], [7], thus maximizing the EO effect efficiency [4] and minimizing the $V_\pi L$ product, estimated as 500 V·μm for SOH modulators against a record value of 50 V·μm in the POH case [8, Table I]. On the other hand, plasmonic modulators exhibit a larger optical insertion loss compared to more conventional solutions, because of the strong intrinsic plasmonic losses and the need to perform photonic–plasmonic mode conversion [5].

Several plasmonic-based modulating devices exploiting different EO materials have been proposed in the recent past, such as the POH MZ modulator [4], [5], [9] based on POH plasmonic phase shifters [10], the POH plasmonic ring modulator [11], the plasmonic directional coupler (PDC) modulator based on ITO [12], [13] or on EO organic materials [14]–[16].

The operation principle of PDC modulators is similar altogether to the one of other DC modulators that have been proposed as an alternative to MZ modulators both in III-V technologies [17], [18] and on lithium niobate, in concentrated [19] or traveling-wave [20] form. With respect to MZ solutions, DC modulators exhibit some interesting features, like the possibility of dual complementary output and of achieving zero or bias-tunable positive or negative chirp [21].

This paper presents a detailed study of coupled-slot coplanar PDC EO modulators, whose aim is to show that a PDC modulator with interesting performance can be implemented with layout and fabrication processes similar altogether to those presented in [4], [5], [22] for the realization of POH coupled-slot MZ modulators.

The paper is structured as follows. The proposed modulator structure is introduced in Section II, where its operating principle and main features are discussed, also in comparison with MZ modulators. Using as a case study a device whose cross section
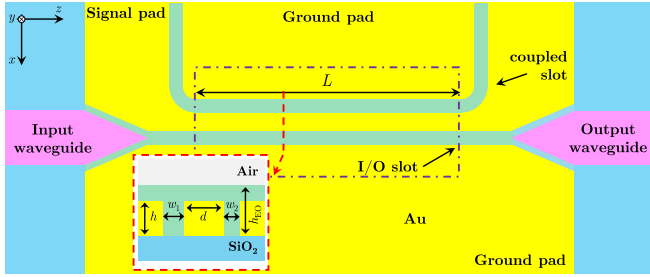
Fig. 1.   Geometry of the device under investigation. The main figure reports the xz top view for y corresponding to the slot center. The inset reports the xy cross-section indicated by the red dashed line. Each color indicates a different material: the NLO polymer DLD-164 is green, air is gray, Au is yellow, SiO$_2$ is dark blue, Si is lilac. The DLD-164 layer only extends to the straight portion of the device of length L marked by the dash-dotted rectangle.

TABLE I
REFRACTIVE INDICES USED IN THE SIMULATIONS

Material	n_{RF}	n_{opt} @ 1.55 μm
Au	–	$0.2524 - j10.4386$ [5]
SiO$_2$	1.97 [31]	1.44 [5]
DLD-164	2.01	1.83 [5]

TABLE II
FIXED GEOMETRICAL PARAMETERS

Quantity	$\overline{w}$	h	h_{EO}
Value, unit	100 nm	220 nm	300 nm

is inspired to the coupled-slot POH MZ modulator presented in [4], similar to the one proposed in [16], where a preliminary feasibility study is provided on the basis of 3D-FDTD simulations, Section III describes the efficient modeling approach exploited for a systematic design and optimization of the PDC modulator. In Section IV a few design case studies are described for both symmetric- and asymmetric-slot structures, and an estimate is made of the sensitivity of the modulator performance to variations of the geometrical parameters (Section IV-B), of the optical and electrical bandwidths (Sections IV-B and IV-C, respectively), of the energy comsumption per bit (Section IV-C), and of the modulator chirp (Section IV-D). The analysis in Section IV confirms that PDC modulators exhibit interesting performance when compared to POH MZ modulators. Conclusions are finally presented in Section V.

II. PLASMONIC COUPLED-SLOT MODULATOR GEOMETRY AND OPERATION PRINCIPLE

DC modulators generally exploit two coupled optical waveguides, where coupling can be controlled externally. In the implementation described in this paper, coupling is controlled through the EO effect, i.e., by varying the refractive index in the slot waveguides through the application of an electric field, induced by the input voltage. In principle, the device has two input and two output ports, since it allows both *through* and *cross-coupling* transmission to the output port. For the sake of definiteness, we will mainly focus on the *through* configuration, where the input and output ports are located on the same plasmonic slot; the performance of the cross-coupling configuration, which is complementary as far as the EO response is concerned, but with different chirp [21], will also be mentioned.

The layout of the PDC EO modulator under investigation is shown in Fig. 1. Each color indicates a different material, whose refractive index is reported in Table I.[1] The main figure reports

a top view of the device, with an inset representing the xy cross-section indicated by the red dashed line. As shown in the inset, the device is fabricated on a SiO$_2$ layer, grown on a Si substrate (omitted in the figure). On top of the SiO$_2$ layer, three parallel Au pads are deposited, one connected to the input voltage source, comprising the radiofrequency (RF) modulating signal and the DC bias, the other two connected to ground. The shape of these contacts is designed in such a way as to obtain two single-mode plasmonic slot waveguides between them. As shown in Fig. 1, which is a y-cut with y corresponding to the middle of the slot, the plasmonic slot waveguide having width w_2 is denoted as the *I/O slot*, since it is connected to two dielectric (photonic) waveguides, from which the input signal is provided (left) and the output signal is extracted (right) at the *through* port. The slot having width w_1 is referred to as the *coupled slot*, that is assumed to be matched at the output (*cross-coupled*) port.[2] The two slots, both having height h, are separated by a gold ridge having width d, and are designed to be parallel for the length L. The plasmonic slots are filled by the DLD-164 EO material [22], [23], having thickness h_{EO} measured from the surface of the SiO$_2$ layer. Table II reports the geometry parameters that are not going to be changed in this investigation. In particular, the average slot width $\overline{w} = (w_1 + w_2)/2$ is chosen as 100 nm (following [4], [5], [9], [10]) in order to obtain a strong EO effect already at low applied voltage while keeping the structure feasible from a fabrication standpoint, and h has been designed to be 220 nm to guarantee that each slot, considered individually, exhibits only the fundamental plasmonic mode along the vertical direction.

As already suggested in the simulation study [14] for a different coupled-slot plasmonic modulator structure, the device in Fig. 1 can be properly designed to operate as an EO amplitude modulator. To demonstrate its principle, Fig. 2 presents the squared magnitude of the electric field for an example of a properly designed modulator, simulated with the 3D finite-difference time-domain (FDTD) commercial software Lumerical [25], in OFF (top) and ON (bottom) conditions. The two conditions differ due to the variation of the slot refractive index induced by the input voltage V_{in}, defined as the sum of the DC bias point V_{DC} and the RF signal V_{RF}, which controls the slot coupling.

---

[1]No specific information has been found on the RF permittivity of the DLD-164 EO chromophore-loaded polymer [22], [23]. In order to have a rough estimate, we considered the dispersion behaviour of the commercial EO polymer SEO125 from Soluxra LLC described in [24], where it is shown that the RF refractive index is 10 % greater than that at optical frequencies. Notice, however, that the static refractive index significantly impacts only the dynamic properties of the device, i.e., the modulation bandwidth, see Section IV-C.

[2]Matching could be obtained by suitably extending the coupled line beyond the output port with a meander slot line, exploiting the high plasmonic losses and keeping a compact footprint. Alternatively, the coupled line could be terminated by a plasmonic-photonic converter (as in the through line) connected with a photonic taper aimed at radiating the output power. In 3D simulations the port is terminaned by absorbing boundary conditions.
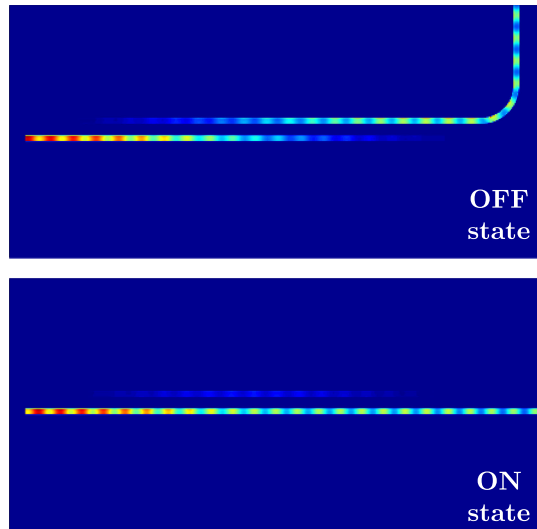
Fig. 2. Squared magnitude of the optical electric field (in arbitrary units, where blue corresponds to zero field), for the xz top view for y corresponding to the slot center, of a symmetric PDC modulator simulated with 3D-FDTD. The top and bottom plots are obtained in the OFF and ON states, respectively. For a cross-coupling modulator configuration, the OFF and ON states will be exchanged.
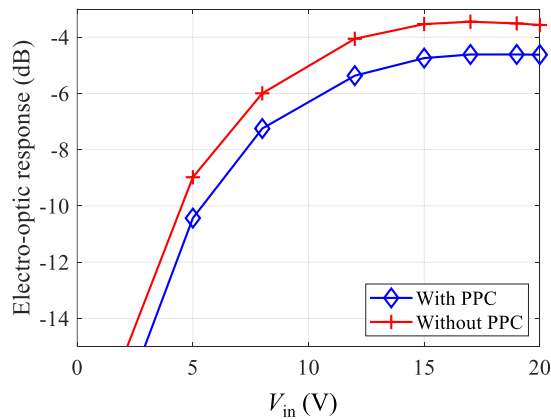

Fig. 3. Normalized EO response of the PDC modulator of Fig. 2. The blue and red curves are obtained with two different sets of 3D-FDTD simulations including and neglecting the PPC section, respectively (details in the text).

At V_{OFF}, all the input power is coupled to the *coupled slot*, thus extinguishing the power in the output section of the *I/O slot*. For the same modulator, Fig. 3 reports the electro-optic response, evaluated as the of output-to-input power ratio at the modulator *through* output port. The figure reports two curves, which have been obtained with two different choices of the I/O terminations in the 3D-FDTD simulation. The blue curve is obtained simulating the entire device, including a silicon input waveguide ($n = 3.6$), with x- and y-widths $W_x = 450$ nm, $W_y = 200$ nm, and photonic-plasmonic converters (PPCs) consisting in triangular tapers extended 200 nm in the z direction and designed in such a way as to keep a constant distance of 50 nm from the corresponding oblique taper in the dielectric waveguide [16]. The red curve is obtained launching directly the plasmonic mode into the input of the plasmonic *I/O slot* and measuring the power at its output, *i.e.*, neglecting the PPC
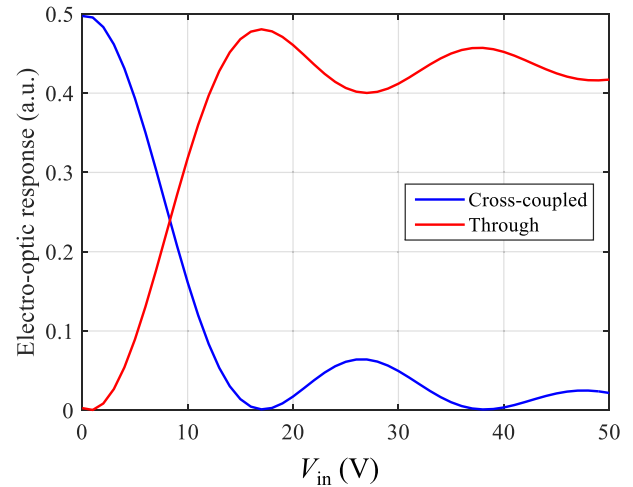

Fig. 4. Normalized EO response of PDC modulator for positive applied voltage: through port (red line); cross-coupled port (blue line). The modulator slot widths w_1 and w_2 are both 100 nm, with $d = 150$ nm, and length $L = 6.8\ \mu$m.

section and the corresponding losses. It is to be noted that the blue and red curves are almost parallel in logarithmic scales, suggesting that the overall (input and output) coupling losses amount to ≈ 1 dB.

For a symmetric PDC modulator, as in the case of Fig. 3, the OFF state, corresponding to maximum coupling, is achieved at $V_{\text{OFF}} = 0$, provided that the length L is chosen properly. Conversely, at V_{ON}, coupling to the *coupled slot* is suppressed due to the refractive index asymmetry induced by the applied field, and the power remains in the *I/O slot*, thus reaching its output section (ON state). An asymmetric design allows, as discussed in Section IV, to shift, virtually without any change, the EO response along the input voltage axis, *e.g.,* in such a way as to place the half-power state at zero input voltage. An example of EO response for a symmetric modulator is shown in Fig. 4; the complementarity of the through port and cross-coupled port responses is clearly visible. Contrarily to the MZ case, the EO response is not periodic in the input voltage, since for $|V_{\text{in}}| > |V_{\text{OFF}}|$ coupling is increasingly suppressed, leading to ripples in the response only.

The modulation principle of this device is therefore completely different from that of the plasmonic MZ modulator [4], [5], [9]. In such modulators, a two-slot plasmonic waveguide is excited with an even input optical field. If the structure is symmetrical and no voltage is applied, the even-mode excitation travels to the output combiner, where positive interference allows for the excitation of the output Si photonic waveguide (ON state). The ON-state insertion loss (IL) is due to both the attenuation of the plasmonic mode and to the coupling losses of the input divider and the output combiner.

At an applied voltage equal to V_π, the phase difference between the fields excited into the two MZ slots leads, in the output combiner, to destructive interference, *i.e.*, to the OFF state with (ideally) zero output optical power. However, the ON/OFF power ratio (extinction ratio, ER) is affected both by the slot asymmetry (that can be useful in shifting the half-power bias

value to zero bias, see [4], but may lead to a different optical power being carried by the two slots), and by the coupling between the two slots. A laterally compact design like the one in [4], [5], with a comparatively narrow ridge between the two slots, leads to modal coupling and to a decrease of the ER, as discussed in [26, Sec. 3.2]. Notice that the effect of mode coupling is always present, also in a MZ with symmetrical slots. In fact, while for zero applied voltage the structure is strictly symmetrical and the coupled slots host an even and an odd mode, only the even one being excited at the MZ input, the application of an input voltage causes the refractive index of the EO material to be different in the two slots, thus leading to an increased mode localization in each slot, and therefore to quasi-even and quasi-odd mode input excitation. As a result, in the OFF state the input even excitation can be decomposed in two modes whose superposition at the modulator output slots includes an odd part (to be radiated at the combiner) but also an even part (that is transmitted to the output photonic waveguide). Under this respect, slot coupling, while allowing for a more compact layout of the modulator, leads in principle to a worse ER. Decreasing coupling, as done in the wide-ridge layout in [9],[3] allows for an improvement of the ER (as discussed in Section IV) but at the same time increases the length and therefore the losses in the splitter and combiner. Representative values for such coupling losses can be found in [5, Fig. 11], where two splitter and combiner solutions are discussed for slots separated by a narrow ridge, with loss of approximately 3 dB and 1 dB, respectively (leading to a total coupling loss of 6 dB and 2 dB), while in [9], where a wide ridge is introduced separating the two slots, the losses in feeding waveguides and PPCs are estimated as 3 dB. Conversely, as already mentioned, 3D simulated values of total PPC losses for the PDC modulator are as low as 1 dB.

With respect to MZ solutions, coupled-slot based modulators follow a different design criterion, since slot coupling is essential for their operation, and therefore a laterally-compact layout is indispensable. Moreover, they may achieve a better output signal extinction in the OFF state, which is not negatively affected by slot asymmetry, and exploit a simpler input and output PPC structure. The simulation study presented in the following sections aims at presenting design criteria for the PDC EO modulator, with result that support the above preliminary conclusions.

III. MODELING STRATEGY OF PDC-BASED EO MODULATORS

To model the EO response of PDC modulators, two simulation steps are required for each V_{in}. The first is the evaluation of the modulating field, which changes the optical dielectric permittivity of the electro-optic material according to

$$\varepsilon_{EO}(x,y,z) = (n_{EO} + \Delta n_{EO}(x,y,z))^2, \qquad (1)$$

where ε_{EO} is the element of the permittivity matrix relating the optical electric field along the poling direction with the displacement field along the same direction. Because the modulator

[3]In [4] an experimental value ER = 6 dB for a ± 3 V swing is reported for a narrow-ridge asymmetric slot MZ [4] while in [9] a DC ER > 25 dB is quoted for a wide-ridge symmetric MZ.

footprint is much smaller than the RF wavelength, even in the case of THz operation ($L \approx 10$ μm against $\lambda_{RF} = 300$ μm at 1 THz), the electrical analysis reduces to a quasi-static problem. This enables to evaluate Δn_{EO} as [27]:

$$\Delta n_{EO} = \frac{1}{2} r n_{EO}^3 \mathcal{E}, \qquad (2)$$

where r is the component of the electro-optic tensor that affects n_{EO} due to an electric field $\mathcal{E}$, directed along the poling direction and with intensity controlled by the voltage V_{in} applied to the ridge. In the calculations presented in this paper we use $r = 180$ pm/V [22]; in RF simulations, Au is treated as an impedance boundary condition, with conductivity $\sigma_{Au,RF} = 410$ kS/cm [28]. The second step requires to perform an optical simulation of the modulator, including the voltage-dependent Δn_{EO} evaluated through (1) and (2) from the quasi-static simulations. The voltage-dependent modulator EO response is then evaluated as a post-processing of the optical simulation.

The most complete simulation framework one may envision is based on 3D simulations of the whole device [29]. For the quasi-static (electrical) step, 3D simulations could be performed with commercially-available codes, e.g., Sentaurus Device by Synopsys [30]. For the optical step, one of the most flexible tools is FDTD, which allows to evaluate the modulator response as the fraction of scattered field coupled to the fundamental mode of the output photonic waveguide. Moreover, as demonstrated by the results reported in Fig. 2, it is possible to evaluate the optical field in every point of the 3D lattice, thus providing a complete picture of the device operation. On the other hand, such 3D simulations require huge computational time and resources even using coarse mesh discretizations that, although capable of capturing the plasmonic character of the slot waveguides, cannot be used for extensive computer-aided design based optimization. Indeed, the mesh is very critical for studying devices involving plasmonic waveguides, since a very fine discretization is required even just to correctly predict their dispersion characteristics. Since a 3D simulation of the entire devices appears not to be practically applicable for computer-aided design, a simpler, yet much more computationally-affordable model is proposed, which is described in the rest of this section.

As suggested by Fig. 3, the PPC losses do not depend significantly on V_{in}, hence they can be included *a posteriori*. Moreover, mode coupling, which is at the basis of the PDC modulation mechanism, only occurs when the slot waveguides are parallel, *i.e.*, in the length L indicated in Fig. 1. It is therefore possible to reduce the problem to a 2D problem. The results presented hereafter have been obtained following this strategy. First, this requires to neglect the z-dependence in (1), which, however, could arise only from second-order effects such as fluctuations of the slot width/height. Under this assumption, the RF field can be evaluated in the xy cross-section through a 2D solver [32]. As an example, the top panel of Fig. 5 reports the x-component, which is dominating in the slot, of the simulated RF field profile for a geometry with $w_1 = w_2 = 100$ nm, spaced by $d = 100$ nm. It is to be remarked that, inside the slots, the simulations fit quite well the approximate formula $\mathcal{E}_x = V_{in}/w$, w being the slot width. This result is used to evaluate $\Delta n_{EO}(V_{in}, x, y)$ with (2), later
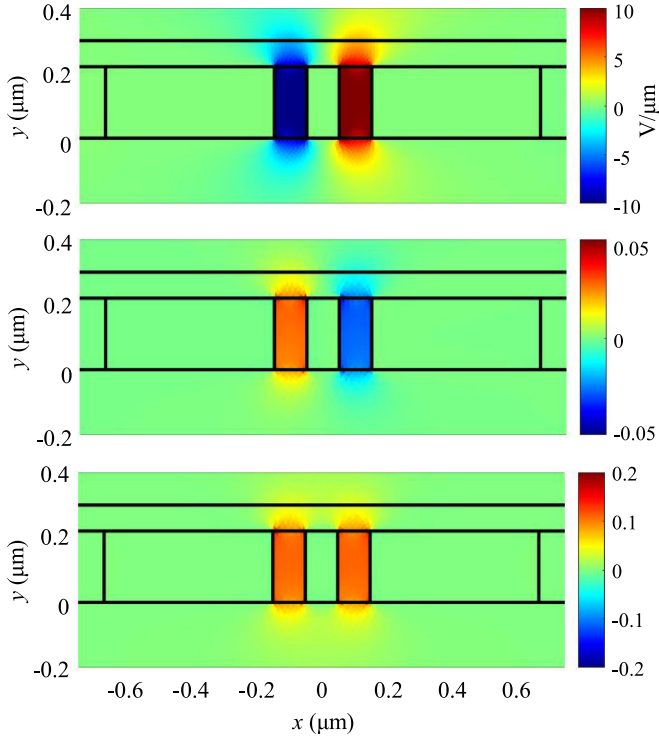
Fig. 5. Examples of x-components of electric field profiles. The top panel reports the RF electric field (units V/μm) for $V_{\rm in} = 1$ V. The center and bottom panels report the real parts of the odd and even optical mode profiles (arbitrary units), respectively.

plugged in (1), and finally used as an input of the 2D optical mode solver [33]. The center and bottom panels of Fig. 5 report, for the same device of the top panel and in the case $V_{\rm in} = 0$, the real part of the x-components of the optical mode field profiles, which, in this case, are odd and even, respectively. The imaginary part, not reported here, exhibits the same behavior. The figure allows to appreciate how, thanks to the localized nature of the plasmonic modes, the overlap with the RF field is excellent, maximizing the electro-optic interaction.[4]

In addition to the plasmonic mode profiles, the optical simulations allow to evaluate the complex propagation constants $k_i = \beta_i - {\rm j}\alpha_i$, $\beta_i = k_0 n_{{\rm eff}\,i}$ and α_i being the propagation and attenuation constants for the i-th mode ($i = 1$ or 2), and the corresponding voltage-dependent mode profiles $|V_i\rangle$. In order to assess the modulator response exploiting these results, we extend the approach presented in [26]. The idea is to express the input field of the modulator, $|I\rangle$, as a linear combination of the voltage-dependent plasmonic modes. In coupler modulators, $|I\rangle$ is the mode of the *I/O* waveguide considered as isolated from the rest of the device. So, we have

$$|I\rangle = c_1^{({\rm I})} |V_1\rangle + c_2^{({\rm I})} |V_2\rangle , \qquad (3)$$

where the coefficients $c_i^{({\rm I})}$ of the linear combination can be evaluated through the projection-based method described in Appendix A. Having expressed the input field in terms of the natural modes of the cross-section, the field at the modulator end, $|O\rangle$, can be evaluated by propagating the coefficients with the appropriate complex propagation constants:

$$|O\rangle = c_1^{({\rm I})} {\rm e}^{-{\rm j} k_1 L} |V_1\rangle + c_2^{({\rm I})} {\rm e}^{-{\rm j} k_2 L} |V_2\rangle . \qquad (4)$$

Considering that the input and output sections of the modulator have the same cross section, the modulator response can be evaluated as the fraction of $|O\rangle$ overlapping with the input field $|I\rangle$. In particular, through another projection, $|O\rangle$ can be represented as

$$|O\rangle = c_1^{({\rm O})} |I\rangle + c_2^{({\rm O})} |C\rangle , \qquad (5)$$

where $|C\rangle$ indicates the mode of the *coupled slot* waveguide shown in Fig. 1 but considered isolated from the rest of the device.[5]

IV. DESIGN OF PDC MODULATORS

A. Symmetric and Asymmetric Modulators

Having already fixed *a priori* the height and the average width of the slots, the remaining design parameters for the cross-section are the asymmetry between the slot widths, $\Delta w = w_2 - w_1$, and the width of the ridge, d, which separates the slots. As a first investigation, in Fig. 6 we present the voltage-dependent effective refractive indices, $n_{{\rm eff}1,2}(V_{\rm in})$, resulting from two groups of parametric simulations.

In particular, Fig. 6(a) reports the results of a symmetric modulator, *i.e.*, $\Delta w = 0$, for different ridge widths. All curves show similar trends. For $V_{\rm in} \to 0$, they exhibit stationary points. These are a signature of coupling between the two waveguide modes. Indeed, in absence of mode coupling, the curves would be perfectly straight lines and cross at 0 V. Instead, the linear behaviour appears only for larger voltages, where the two $n_{\rm eff}$ exhibit linear asymptotes. The ridge width d impacts the mode coupling strength: for small d the slots are closer, hence more coupled, as indicated by the larger $\Delta n_{\rm eff}(0) = n_{\rm eff1}(0) - n_{\rm eff2}(0)$. Instead, for distant slots, the effective indices reach the linear regime even for very small voltages. Fig. 6(b) reports the results of simulations performed with $d = 300$ nm, for different width asymmetries. The only effect of the asymmetry appears to be a translation of the curves on the $V_{\rm in}$ axis proportional to Δw, with no visible impact on the mode coupling strength.

By inspecting Fig. 2, it is clear that, in these devices, the extinction mechanism is based on mode coupling. In this view, it is possible to define the OFF state voltage $V_{\rm OFF}$ as the state where $\Delta n_{\rm eff}(V_{\rm OFF})$ is minimum. This is represented in Fig. 7(a), which reports $V_{\rm OFF}(\Delta w)$. The curve is a straight line,

---

[4]The numerical approaches in [32] and [33] have been implemented in MATLAB [34]. First, the RF field is evaluated on proper RF discretization mesh, and $\Delta n_{\rm E}(x, y)$ derived from (2) and (1) is interpolated on a denser (optical) mesh required to accurately compute the plasmonic modes. Additional details about the RF and optical solvers coupling strategy can be found in [26], [29]. All simulations presented in this paper, except the ones in Figs. 2 and 3, have been performed with this modeling strategy.

[5]We may note that this approach, described here for PDC modulators, applies also to MZ modulators. The only difference is that, in MZ modulators, the splitter excites the two slots in the same measure, so that $|I\rangle$ and $|C\rangle$ are quasi-even and quasi-odd modes (including possible slot asymmetries). Then, the output response has the physical meaning of the even fraction of $|O\rangle$, *i.e.*, the only part that is not radiated after reaching the output combiner.
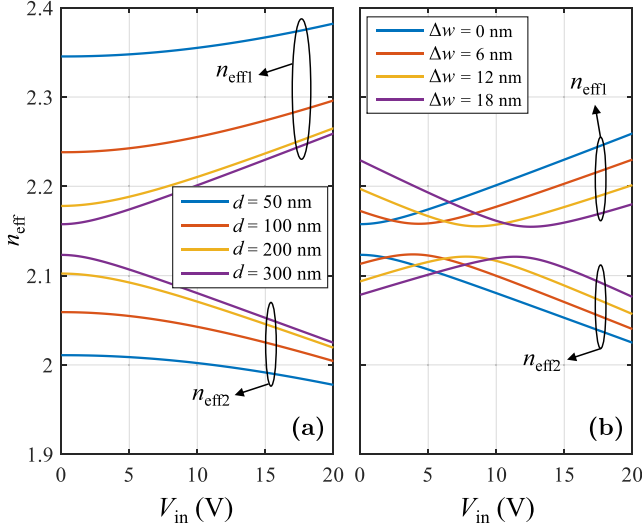
Fig. 6. Voltage-dependent effective refractive indices. Each pair of top and bottom curves with the same color indicates n_{eff1} and n_{eff2}, respectively. The left (a) panel results from a parametric investigation for fixed slot asymmetry $\Delta w = 0$ and changing the ridge width d. The right (b) panel is obtained from a parametric investigation for fixed $d = 300$ nm ridge width and changing the slot asymmetry Δw.

Fig. 8. Cuts of the optical field component E_x performed at y corresponding to the slot center, of the waveguide modes $|V_1\rangle$ and $|V_2\rangle$, input field $|I\rangle$, and output field $|O\rangle$, for a symmetric modulator with $d = 150$ nm and $L = 6.8$ μm at the OFF state voltage $V_{\text{in}} = 0$. Blue and red curves indicate the real and imaginary parts of the field profiles. The small spurious field in the left waveguide is indeed a numerical artifact; it has been verified that it does not affect the final results.
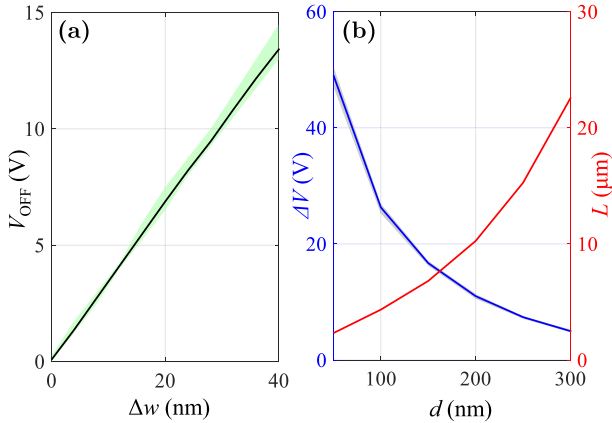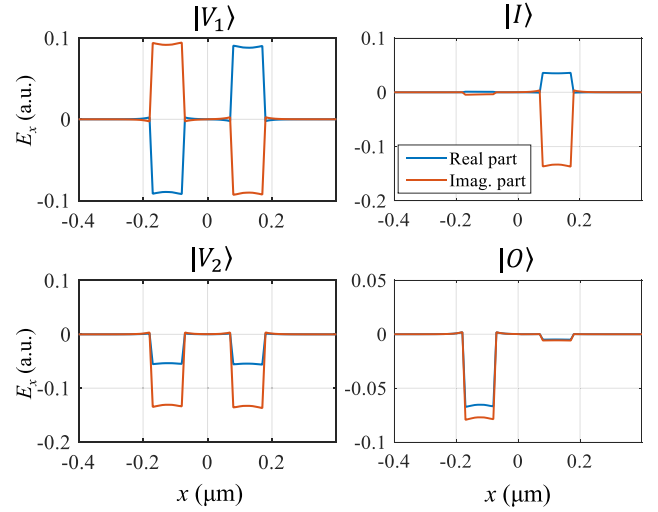

Fig. 7. Design plots for coupler modulators. Left (a) panel: OFF state voltage V_{OFF} versus the slot asymmetry Δw; the green shading indicates the sensitivity of V_{OFF} to the ridge width d, varied in the range $[50 \div 300]$ nm. Right (b) panel: ON-OFF state swing ΔV (blue curve and shading) and L (red curve and shading) versus d, varying Δw as a parameter in the range $[0 \div 40]$ nm. The red shading is almost invisible, demonstrating the very weak dependence of L on the slot asymmetry.

further demonstrating the proportionality of the horizontal shift of the curves of Fig. 6(b) to Δw. This plot presents also a green shading, which corresponds to varying the ridge width d as a parameter: this shows that V_{OFF} exhibits a weak dependence on it. In this view, Δw can be chosen according to the targeted OFF-state voltage.

There are two parameters left to complete the modulator design: the ridge width d, and the modulator length L. However, the two parameters are related, as the red curve in Fig. 7(b) clearly suggests. This behaviour can be better understood by considering the modal field distributions in the coupled slots. To this aim, Fig. 8 shows cuts, at y corresponding to the slot center, of $|V_1\rangle$, $|V_2\rangle$, $|I\rangle$, and $|O\rangle$, for a symmetric modulator

with $d = 150$ nm, at $V_{\text{in}} = 0$, where mode coupling is strongest (so that $V_{\text{OFF}} = 0$). The $|V_1\rangle$ and $|V_2\rangle$ plots in Fig. 8 stress another signature of mode coupling, i.e., the fact that the mode profiles at $V_{\text{in}} = 0$ are odd ($|V_1\rangle$) and even ($|V_2\rangle$). (On the other hand, for large V_{in}, it could be seen that the mode profiles tend to be localized in either slot.) These modes are sorted in decreasing order by their energy, $|V_1\rangle$ being the mode with larger effective refractive index. From a careful inspection of the top-right panel of Fig. 8, one could notice a small spurious field in the left waveguide. This is related to the fact that the coefficients $c_i^{(\text{I})}$ of the linear combination defining $|I\rangle$ in (3) are obtained with a 2×2 least-squares optimization performed over the entire cross-section (see Appendix A), so minor local errors are in order. The very low ER achievable with this method (see, e.g., Figs. 3 and 9) suggests that this artifact should not affect significantly the predictions.

On the top-right panel $|I\rangle$ is reported, represented as a linear combination of $|V_1\rangle$ and $|V_2\rangle$ as in (3). Due to the aforementioned symmetries, it is understood that $|I\rangle$ excites $|V_1\rangle$ and $|V_2\rangle$ with the same magnitude. At the output section, i.e., after the two modes propagate for a length L, the relative phase-shift:

$$\Delta\phi(V_{\text{in}}) = k_0 \, L \Delta n_{\text{eff}}(V_{\text{in}}), \qquad (6)$$

is introduced. If $\Delta\phi(V_{\text{OFF}}) = \pi$, then, at the output section, the excitation coefficients have opposite sign with respect to the input section, leading to a field localized in the left slot only. This is the case of the bottom-right plot of Fig. 8, resulting in a modulator length designed as

$$L = \frac{\pi}{k_0 \, L \Delta n_{\text{eff}}(V_{\text{OFF}})}. \qquad (7)$$

With the data in Fig. 8, we obtain $L = 6.8$ μm. Obviously, the L value in (7) could be generalized using an odd multiple of π,
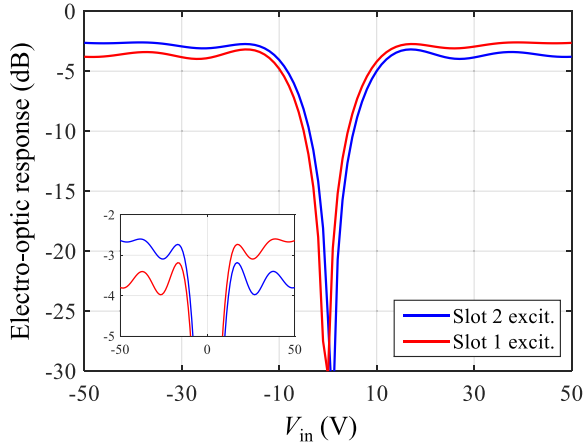
Fig. 9. EO response of the symmetric PDC modulator of Fig. 8 ($d = 150$ nm, $\Delta w = 0$, $L = 6.8$ μm), evaluated as the coefficient $c_1^{(O)}$ from (5). The blue curve refers to the same excitation scheme of Fig. 8. The red curve is obtained exciting the left slot, *i.e.*, by exchanging the *I/O* and *coupled* slots.

i.e., $(2n + 1)\pi$, but this choice is not convenient, since it would lead to longer modulators and to higher ON-state losses.

Equation (7) allows to obtain the relation $L(V_{\text{OFF}})$ shown in Fig. 7(b). Just like the left panel, this is a parametric plot on Δw; yet, the impact of Δw is negligible. Fig. 7(b) also includes (blue curve), the voltage swing required $\Delta V = |V_{\text{ON}} - V_{\text{OFF}}|$. V_{ON} is defined as the voltage at which the modes excited in the input section recombine in phase at the output section, *i.e.*, such that the phase shift (6) is equal to 2π (notice that the definition is not critical, since for $|V_{\text{in}}| > |V_{\text{ON}}|$ the modulator practically remains in the ON state). Also in this case, the dependence on the parameter Δw (shown as a blue shading) is quite weak. This demonstrates that Δw and d are virtually orthogonal in determining V_{OFF} and the set $[\Delta V, L]$, respectively. The opposite trends of ΔV and L vs. d in Fig. 7(b) suggest that the design results from a trade-off. Indeed, modulators with strong mode coupling (small d) are characterized by large $\Delta n_{\text{eff}}(V_{\text{OFF}})$, but also by a weaker dependence of $\Delta n_{\text{eff}}(V_{\text{in}})$. This has a positive impact on L, which can be shorter, but results also in a larger ΔV.

As discussed at the end of Section III, the modulator EO response simply is the coefficient $c_1^{(O)}$ from (5). As an example, Fig. 9 reports the EO response of the symmetric modulator presented in Fig. 8. From the blue curve, the insertion loss (IL, about 4 dB) can be obtained as the EO response at the ON state, corresponding to a voltage 15 V; the computed ER (*i.e.*, the ratio of the OFF and ON responses, the former occurring at $V_{\text{in}} = V_{\text{OFF}} = 0$ V) is in excess of 25 dB. On the other hand, it can be shown (by means of calculations similar to those described in Section III) that the ER of a POH MZ modulator varies almost linearly from 0 dB to 25 dB for d increasing from 100 nm to 500 nm (the upper limit of this interval is consistent with the value $d = 410$ nm reported in [4, Supplementary information, Table S 1]). Indeed, as discussed in [26, Sec. 3.3], mode coupling is a detrimental effect in MZ modulators, impacting in particular on the ER, while the PDC modulator shows a computed ER well in excess of 25 dB on the whole d interval.

The EO response has been simulated over a broad V_{in} range (extending well beyond $|V_{\text{ON}}|$) to emphasize some peculiar features of PDC modulators. This is shown in the inset of Fig. 9. As already noticed, contrarily to the MZ modulator whose EO response is periodic, only one ON state is present, with two OFF states corresponding to $V_{\text{OFF}} \pm \Delta V$. Indeed, the extinction mechanism of PDC modulators is based on mode coupling, which is strong only at V_{OFF}; for $|V_{\text{in}}| > |V_{\text{OFF}} \pm \Delta V|$, the field profiles are increasingly localized in the slots and no stationary points are encountered in the $n_{\text{eff}\,i}(V_{\text{in}})$ characteristics. However, since complete mode localization is only achieved for $V_{\text{in}} \to \infty$, implying that the PDC is in the ON state independent on the device length L, for finite L response maxima still imply a constructive interference of the even and odd mode components, which only occurs, for a given L, at specific values of V_{in}. The increase in localization with increasing V_{in} leads to a decrease of the amplitude in the response ripples. Finally, notice that, for the symmetric device, the maximum applied voltage is of the order of 20 V, corresponding to a maximum field in the DLD-164 polymer of the order of 200 V/μm, still compatible with the material breakdown field, which exceeds 250 V/μm in DC, see [35, Fig. 2]. The V_{ON} and V_{OFF} ranges discussed here are also compatible with those of experimentally realized POH MZ modulators [4], [5]. Moreover, an asymmetric coupler design allows to shift to $V_{\text{DC}} = 0$ the half-amplitude bias point, thus reducing by a factor of 2 the maximum electric field in the slot.

Another peculiarity of PDC modulators are the asymmetries arising for $V_{\text{in}} \gtrless V_{\text{OFF}}$. Consider for instance the blue curve in Fig. 9, corresponding to excitation in the right slot as presented in Fig. 8: the IL for $V_{\text{in}} > V_{\text{OFF}}$ is about 1 dB larger than that for $V_{\text{in}} < V_{\text{OFF}}$. Even if the slots are symmetric, *i.e.*, $\Delta w = 0$, the device is not symmetric due to the fact that one slot only is excited at the input. In this view, positive or negative voltages lead to opposite EO effect, leading to different group velocity, losses and mode profiles. The red curve, corresponding to left-slot excitation, exhibits an opposite behaviour. This points out that there is an optimum excited slot, to be chosen coherently with the modulator bias voltage.

B. Parametric Sensitivity and Optical Bandwidth

In MZ modulators, extinction is obtained through destructive interference at the output of the phase shifters, and the $V_{\pi}L$ product depends on the cross-section geometrical parameters. This implies that the OFF state can be always obtained (albeit with non-ideal extinction), independent of L, with a suitable V_{π}. On the other hand, in PDC modulators, L has to be designed according to (7) and/or Fig. 7(b) to have extinction at a certain V_{OFF}.

To assess to which extent this design constraint is critical vs. variations of the modulator geometry, Fig. 10 presents the results of an investigation versus the parameter L. (Notice that, since the modulator length L depends on the design wavelength, the performance sensitivity with respect to L also is a limiting factor for the optical bandwidth.) The analysis has been performed on a modulator with $d = 150$ nm, targeted to be similar, in terms of
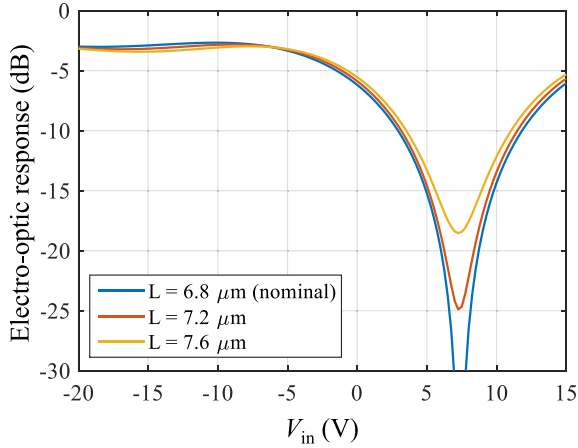
Fig. 10. EO response of the coupler modulator with $d = 150$ nm and $\Delta w = 20$ nm, for different length L. The solid blue curve, referring to $L = 6.8$ μm, is the reference design following (7).

Fig. 11. Sensitivity investigations of the EO response of the symmetric PDC modulator of Fig. 8 ($d = 150$ nm, $\Delta w = 0$, $L = 6.8$ μm) to $w_{1,2}$ (dash-dotted curves) and h (dashed curves). The dash-dotted curves are obtained for $w_1 = w_2$. The response of the nominal device is reported with the solid black curve for reference.

Fig. 12. Behaviour of the EO response for different operation wavelengths around 1550 nm for the reference structure in Fig. 11.

mode coupling (hence, with the same L), to that presented in the previous section, but with a slot asymmetry $\Delta w = 20$ nm. This choice of parameters sets the half-power point in $V_{\text{in}} = 0$ V: the IL is about 3 dB, and the half-power bias point (corresponding to ≈ -6 dB level) is at about 0 V. This is consistent with Fig. 7, since this choice leads to $V_{\text{OFF}} \approx 8$ V and $\Delta V \approx 16$ V, the half-power point being approximately midway the OFF and ON voltages. This allows to design the PDC bias around the quadrature point (where linearity is maximum) at zero bias voltage, so that the ON-OFF condition can be reached with a halved V_{in}, with consequent advantages in terms of energy-per-bit, stability of the polymer (due to the reduced maximum field) but also simplicity of the driving electronics (since $V_{\text{DC}} = 0$ no bias-T is required). Fig. 10 suggests that the exact value of L is not very critical, since -22 dB levels are still possible with ± 400 nm variations with respect to the nominal length $L = 6.8$ μm (it has been verified that similar results hold for shorter L, i.e., $L = 6.4$ μm and $L = 6.0$ μm).

Fabrication issues may also affect the width and height of the plasmonic slots [22]. For the widths, [9] indicates that the lateral uncertainty is ± 10 nm. Such fluctuations could either introduce asymmetries between the two slot widths, or change both widths in the same way. For the former case, Fig. 7 demonstrates that a slot asymmetry leads only to a change of V_{OFF}, without requiring to re-design L. This is also clear from Figs. 9 and 10, which are obtained for designs differing only for Δw. Fig. 11 presents a sensitivity analysis for fluctuations in w_1 and w_2 having the same value (dash-dotted lines). It is apparent that, with respect to the reference device (solid blue curve), this case does not lead to any appreciable difference. Indeed, even if n_{eff1} and n_{eff2} change, their difference is almost constant in the strong mode coupling regime (i.e., for V_{in} close to the V_{OFF}), at least for small variations in the individual slot widths. The dashed curves of Fig. 11 finally report an investigation of the sensitivity of the EO modulator response with respect to h. This suggests that this parameter does affect the ER of the device, which could be ascribed to a change of Δn_{eff}, so that the nominal L does not longer guarantee $\Delta \phi = \pi$ at the designed V_{OFF}. For a ± 10 nm variation, however, an ER in excess of 20 dB is anyway obtained.
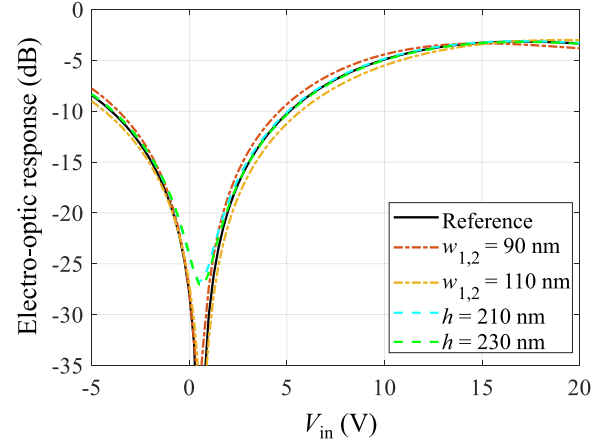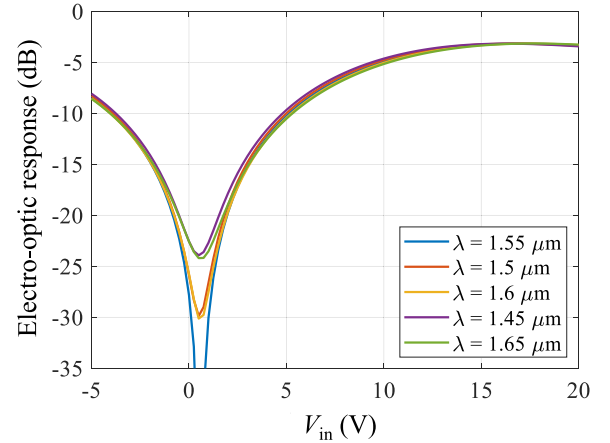
Changes in the operating wavelength vs. the nominal (design) value lead to a variation of the L/λ ratio, with effects, as already stressed, similar to a variation in L, but also to a variation of the effective index in the plasmonic mode. The analysis on the sensitivity versus L already suggests that the PDC modulator does not exhibit a strongly resonant behavior (as in resonant ring modulators), corresponding to a moderately broad optical bandwidth. This is confirmed by the simulations shown in Fig. 12, showing that the ON state behavior is practically unaffected by varying the operating wavelength, while the ER remains in excess of 27 dB on a 100 nm optical bandwidth, and in excess of 20 dB on a 200 nm optical bandwidth. These values compare favourably with those of the POH MZ modulators, which exhibit a typical optical bandwidth in excess of 100 nm [4].

C. Modulation Bandwidth and Energy Consumption

Since the modulator length is much smaller than the RF wavelength, even assuming THz operation, the PCM frequency response can be approximated with that of the RC circuit shown
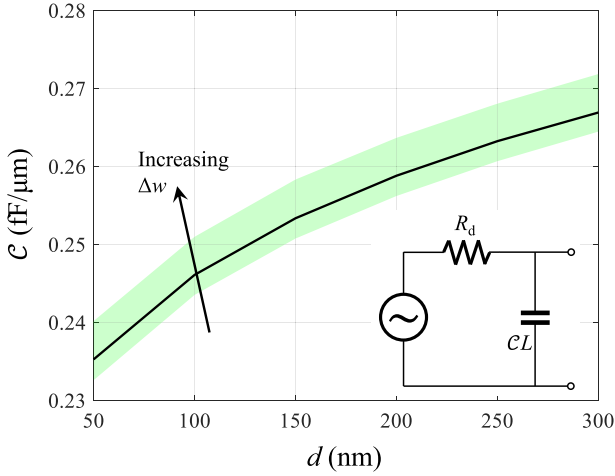
Fig. 13. Per-unit-length capacitance $\mathcal{C}$ of PDC modulators versus d, varying Δw as a parameter in the range $[0 \div 40]$ nm. The black curve is the average value, and the green shading indicates the sensitivity of $\mathcal{C}$ to Δw. The inset reports the RC circuit describing the PDC dynamics.

Fig. 14. Small-signal Henry parameter α_{H} as a function of the bias point for the through port (blue curve) and the cross-coupled port (red curve). The modulator geometry is that of Figs. 8 and 9.

in the inset of Fig. 13, R being the device and driver total equivalent resistance and C its capacitance. It has been verified, by quasi-static simulations [32], that the device resistance is negligible compared to the typical $R_{\mathrm{d}} = 50\,\Omega$ high-frequency driver resistance, and that its capacitance is frequency-independent. More in detail, Fig. 13 reports a parametric study of the per-unit-length capacitance $\mathcal{C}$ (such that $C = \mathcal{C}L$) of PDC modulators for $\Delta w \in [0, 40]$ nm. These results demonstrate that $\mathcal{C}$ depends weakly on Δw, and shows a moderate increase with d in the design range.

In the parameter range investigated in this work, $\mathcal{C}$ is lower than 0.28 fF/μm. Using this as an upper bound and considering a modulator length $L = 7\ \mu$m, bounds can be estimated for the intrinsic device bandwidth and energy-per-bit consumption. Starting from the former, the intrinsic cutoff frequency $f_{\mathrm{c}} = 1/(2\pi\tau)$ can be evaluated from the time constant $\tau = RC$, resulting to be about 1.6 THz (not considering possible parasitic capacitances external to the device). As for the POH modulator in [4], the extrinsic device bandwidth is expected to be dominated by external parasitics. For what concerns the power consumption, it can be quantified by the energy-per-bit, which can be approximately estimated with the expression [35], [36]:

$$W_{\mathrm{bit}} = \frac{1}{4}CV_{\mathrm{RF}}^2, \qquad (8)$$

resulting, for a $V_{\mathrm{RF}} = \pm 3$ V peak-to-peak drive voltage swing, to be about 18 fJ/bit. This compares well with the POH MZ modulator value of 25 fJ/bit reported in [4] for the same peak-to-peak drive voltage swing.

D. Modulator Chirp

The chirp performance of directional coupler based modulators is discussed in [21], where an analytical model, based on the perturbative treatment of coupling between interacting
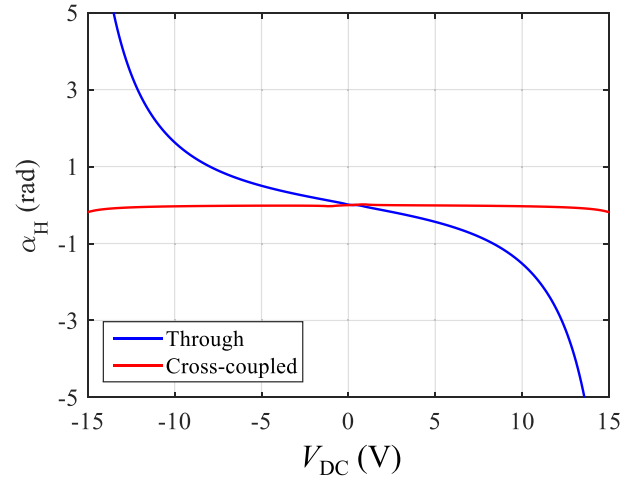
waveguides, is provided for the Henry chirp parameter α_{H}:

$$\alpha_{\mathrm{H}}(t) = 2\frac{\dfrac{\mathrm{d}\phi(t)}{\mathrm{d}t}}{\dfrac{1}{p_{\mathrm{out}}(t)}\dfrac{\mathrm{d}p_{\mathrm{out}}(t)}{\mathrm{d}t}},$$

where $\phi(t)$ is the phase of the output optical field, $p_{\mathrm{out}}(t)$ the optical output power. In the customary bias-dependent small-signal approximation, it is:

$$\alpha_{\mathrm{H}} = 2\frac{\Delta\phi}{\dfrac{1}{P_{\mathrm{out}}}\Delta P_{\mathrm{out}}} = 2\frac{\dfrac{\Delta\phi}{\Delta V_{\mathrm{in}}}}{\dfrac{1}{P_{\mathrm{out}}}\dfrac{\Delta P_{\mathrm{out}}}{\Delta V_{\mathrm{in}}}},$$

where P_{out} is the optical output power at the modulator bias voltage V. According to [21], $\alpha_{\mathrm{H}} = 0$ identically for the cross-coupled modulator while it depends on bias for the through modulator. Values of α_{H} for the half power point in the through modulator, as shown in [21, Fig. 5], are around unity.

The numerical model presented in Section III allows for a straightforward evaluation of the small-signal α_{H}, since it directly provides the bias-dependent output field amplitude and phase both for the through output port (the one considered in the present paper, see Fig. 1) and the cross-coupled port. The results obtained are shown as a function of the applied voltage, for both ports, in Fig. 14. The PDC modulator considered is symmetrical, with $V_{\mathrm{ON}} = 0$, $V_{\mathrm{OFF}} \approx 16$ V and half-power bias around 8 V. In agreement with [21], the cross-coupled port shows very low (albeit not identically zero) chirp, while the through port α_{H} is odd with respect the bias voltage, with half-power values again around ± 1. Contrarily to MZ symmetric modulators (*e.g.,* lithium niobate X-cut modulators), where $\alpha_{\mathrm{H}} = 0$ independent on bias, see *e.g.,* [27], the present analysis confirms that PDC modulators exhibit either zero chirp (in the cross-coupled configuration) or tunable (positive or negative, according to the sign of the bias voltage) chirp, which may be interesting for dispersion compensation.

V. Conclusion

The paper presents a simulation study aimed at assessing the modulation performance of POH EO modulators based on directional couplers. To provide a simulation tool effective for computer-aided design, a simplified approach has been presented, exploiting 2-mode field representations. This methodology has been applied to develop a design strategy for PDC modulators, which has been discussed focusing on representative symmetric and asymmetric devices. Asymmetry has been shown to affect the EO response by a rigid shift on the V_{in} axis, thus allowing to have the half-power bias at $V_{\text{DC}} = 0$ V.

The simulated performance compares well with the one of POH MZ modulators: IL around 4 dB, $V_\pi L$ product (where the equivalent V_π is $\Delta V = |V_{\text{ON}} - V_{\text{OFF}}|$) around 110 V·$\mu$m, ER in excess of 25 dB, THz intrinsic modulation bandwidth, energy consumption of the order of 20 fJ/bit and comparable optical bandwidth in excess of 100 nm. The Henry chirp parameter is negligible (as in ideal symmetric MZ modulators) in the cross-coupled configuration and of the order of unity for the through configuration.

Perspectives for integration in Si photonic integrated circuits are similar to those of POH MZ modulators. Yet, the present analysis suggests that PDCs may have some advantages with respect to MZ modulators. First, because a single slot has to be excited, the launching scheme is simpler, mitigating the photonic-plasmonic conversion losses, that we demonstrate being around 1 dB in the ON state. Secondly, in PDC modulators, reducing the lateral extent of the device (and hence its footprint and capacitance) does not introduce any ER penalty. In conclusion, PDCs appear to be interesting candidates to push further the POH technology towards the attojoule energy-per-bit domain.

Appendix A
Evaluation of the Field Expansion Coefficients

The purpose of this Appendix is to provide additional details on the numerical approach summarized by (3)–(5). The first step regards the evaluation of the coefficients $c_i^{(\text{I})}$. These coefficients are obtained by projecting (3) on the voltage-dependent mode profiles $|V_i\rangle$. This leads to the following system of equations:

$$\underbrace{\begin{bmatrix} \langle V_1|V_1\rangle & \langle V_1|V_2\rangle \\ \langle V_2|V_1\rangle & \langle V_2|V_2\rangle \end{bmatrix}}_{\underline{\underline{A}}^{(\text{I})}} \underbrace{\begin{bmatrix} c_1^{(\text{I})} \\ c_2^{(\text{I})} \end{bmatrix}}_{\underline{c}^{(\text{I})}} = \underbrace{\begin{bmatrix} \langle V_1|I\rangle \\ \langle V_2|I\rangle \end{bmatrix}}_{\underline{b}^{(\text{I})}} \tag{9}$$

where projections are based on the bra-ket product $\langle V_j|V_i\rangle$ defined as

$$\langle V_j|V_i\rangle = \iint \underline{E}_j^*(V_{\text{in}}) \cdot \underline{E}_i(V_{\text{in}}) \, dx \, dy, \tag{10}$$

and the scalar product (performed over the cross-section simulated with the FEM mode solver) involves the transverse (x and y) components of the electric field. The evaluation of the right-hand side is similar, but it involves the projection of the input field $|I\rangle$, which is voltage-independent. Representing the input field as a linear combination of the voltage-dependent modes is advantageous because it allows to evaluate the output

field $|O\rangle$, for each V_{in}, by propagating these coefficients with propagation constants evaluated with the voltage-dependent effective refractive indices, with (4). Assuming that the output field has the same profile of the excitation field, which is the case of both MZ (even mode) and PDC (I/O waveguide mode) modulators, the modulator EO response is evaluated as the fraction of $|I\rangle$ in $|O\rangle$, *i.e.,* the coefficient $c_2^{(\text{O})}$ in (5). These coefficients can be estimated with a procedure similar to that of (9), *i.e.,* by projecting the output field on the fields $|I\rangle$ and $|C\rangle$, leading to the system:

$$\underbrace{\begin{bmatrix} \langle I|I\rangle & \langle I|C\rangle \\ \langle C|I\rangle & \langle C|C\rangle \end{bmatrix}}_{\underline{\underline{A}}^{(\text{I})}} \underbrace{\begin{bmatrix} c_1^{(\text{O})} \\ c_2^{(\text{O})} \end{bmatrix}}_{\underline{c}^{(\text{O})}} = \underbrace{\begin{bmatrix} \langle I|O\rangle \\ \langle C|O\rangle \end{bmatrix}}_{\underline{b}^{(\text{O})}} \tag{11}$$

from whose solution $c_1^{(\text{O})}$ and $c_2^{(\text{O})}$ are obtained.

Disclosures

The authors declare no conflicting interests.

References

[1] G. Sinatkas, T. Christopoulos, O. Tsilipakos, and E. E. Kriezis, "Electro-optic modulation in integrated photonics," *J. Appl. Phys.*, vol. 130, no. 1, 2021, Art. no. 010901.

[2] R. Schmidt and R. Alferness, "Directional coupler switches, modulators, and filters using alternating $\delta\beta$ techniques," *IEEE Trans. Circuits Syst.*, vol. CSI-26, no. 12, pp. 1099–1108, Dec. 1979.

[3] G. T. Reed, G. Mashanovich, F. Y. Gardes, and D. J. Thomson, "Silicon optical modulators," *Nature Photon.*, vol. 4, no. 8, pp. 518–526, 2010.

[4] C. Haffner *et al.*, "All-plasmonic Mach–Zehnder modulator enabling optical high-speed communication at the microscale," *Nature Photon.*, vol. 9, pp. 525–528, Jul. 2015.

[5] C. Haffner *et al.*, "Plasmonic organic hybrid modulators-scaling highest speed photonics to the microscale," *Proc. IEEE*, vol. 104, no. 12, pp. 2362–2379, Dec. 2016.

[6] R. Palmer *et al.*, "Low power Mach-Zehnder modulator in silicon-organic hybrid technology," *IEEE Photon. Technol. Lett.*, vol. 25, no. 13, pp. 1226–1229, Jul. 2013.

[7] R. Palmer *et al.*, "High-speed, low drive-voltage silicon-organic hybrid modulator based on a binary-chromophore electro-optic material," *J. Lightw. Technol.*, vol. 32, no. 16, pp. 2726–2734, Aug. 2014.

[8] C. Koos *et al.*, "Silicon-organic hybrid (SOH) and plasmonic-organic hybrid (POH) integration," *J. Lightw. Technol.*, vol. 34, no. 2, pp. 256–268, Nov. 2015.

[9] W. Heni *et al.*, "108 gbit/s plasmonic Mach–Zehnder modulator with > 70-GHz electrical bandwidth," *J. Lightw. Technol.*, vol. 34, no. 2, pp. 393–400, Jan. 2016.

[10] A. Melikyan *et al.*, "High-speed plasmonic phase modulators," *Nature Photon.*, vol. 8, no. 3, pp. 229–233, 2014.

[11] C. Haffner *et al.*, "Low-loss plasmon-assisted electro-optic modulator," *Nature*, vol. 556, pp. 483–486, 2018.

[12] J. T. Kim, "Silicon optical modulators based on tunable plasmonic directional couplers," *IEEE J. Select. Topics Quantum Electron.*, vol. 21, no. 4, Jul./Aug. 2015, Art. no. 3300108.

[13] J.-S. Kim and J. T. Kim, "Silicon electro-optic modulator based on an ITO-integrated tunable directional coupler," *J. Appl. Phys.*, vol. 49, no. 7, 2021, Art. no. 075101.

[14] M. Y. Abdelatty, A. O. Zaki, and M. A. Swillam, "Hybrid silicon plasmonic organic directional coupler-based modulator," *Appl. Phys. A*, vol. 123, no. 1, 2016, Art. no. 11.

[15] D. C. Zografopoulos, M. A. Swillam, L. A. Shahada, and R. Beccherelli, "Hybrid electro-optic plasmonic modulators based on directional coupler switches," *Appl. Phys. A*, vol. 122, 2016, Art. no. 344.

[16] M. Ghomashi, A. Tibaldi, F. Bertazzi, M. Vallone, M. Goano, and G. Ghione, "Simulation of electro optic modulators based on plasmonic directional couplers," in *Proc. 20th Int. Conf. Numer. Simul. Optoelectron. Devices*, 2020, pp. 9–10.

[17] K. Tada and K. Hirose, "A new light modulator using perturbation of synchronism between two coupled guides," *Appl. Phys. Lett.*, vol. 25, no. 10, pp. 561–562, 1974.

[18] J. C. Campbell, F. A. Blum, D. W. Shaw, and K. L. Lawley, "GaAs electro-optic directional-coupler switch," *Appl. Phys. Lett.*, vol. 27, no. 4, pp. 202–205, 1975.

[19] M. Papuchon *et al.*, "Electrically switched optical directional coupler: Cobra," *Appl. Phys. Lett.*, vol. 27, no. 5, pp. 289–291, 1975.

[20] R. Alferness, C. Joyner, L. Buhl, and S. Korotky, "High-speed traveling-wave directional coupler switch/modulator for $\lambda = 1.32$ μm," *IEEE J. Quantum Electron.*, vol. 19, no. 9, pp. 1339–1341, Sep. 1983.

[21] F. Koyama and K. Iga, "Frequency chirping in external modulators," *J. Lightw. Technol.*, vol. 6, no. 1, pp. 87–93, 1988.

[22] W. Heni *et al.*, "Nonlinearities of organic electro-optic materials in nanoscale slots and implications for the optimum modulator design," *Opt. Exp.*, vol. 25, no. 3, pp. 2627–2653, Feb. 2017.

[23] D. L. Elder, S. J. Benight, J. Song, B. H. Robinson, and L. R. Dalton, "Matrix-assisted poling of monolithic bridge-disubstituted organic NLO chromophores," *Chem. Mater.*, vol. 26, no. 2, pp. 872–874, Jan. 2014.

[24] X. Zhang *et al.*, "Electric field sensor based on electro-optic polymer refilled silicon slot photonic crystal waveguide coupled with bowtie antenna," *Proc. SPIE*, 2013, Art. no. 862418.

[25] *Lumerical Inc.*, 2019. [Online]. Available: https://www.lumerical.com/products/

[26] A. Tibaldi, M. Ghomashi, F. Bertazzi, M. Goano, M. Vallone, and G. Ghione, "Plasmonic-organic hybrid electro/optic Mach-Zehnder modulators: From waveguide to multiphysics modal-FDTD modeling," *Opt. Exp.*, vol. 28, no. 20, pp. 29253–29271, Sep. 2020.

[27] G. Ghione, *Semiconductor Devices for High-Speed Optoelectronics*. Cambridge, U.K.: Cambridge Univ. Press, 2009.

[28] R. A. Serway and J. W. J. Jewett, *Principles of Physics*, 5th ed. Boston, MA, USA: Brooks/Cole, 2012.

[29] A. Tibaldi, M. Ghomashi, F. Bertazzi, M. Goano, M. Vallone, and G. Ghione, "Organic electro-optic Mach-Zehnder modulators: From physics-based to system-level modeling," *Phys. Status Solidi A*, vol. 218, no. 21, 2021, Art. no. 2100390.

[30] *Sentaurus Device User Guide*. Version N-2017.09, Synopsys, Inc., Mountain View, CA, USA, Sep. 2017.

[31] P. R. Gray, P. J. Hurst, S. H. Lewis, and R. G. Meyer, Eds., *Analysis and Design of Analog Integrated Circuits*. New York, NY, USA: Wiley, 2009.

[32] F. Bertazzi, G. Ghione, and M. Goano, "Efficient quasi-TEM frequency-dependent analysis of lossy multiconductor lines through a fast reduced-order FEM model," *IEEE Trans. Microw. Theory Techn.*, vol. MTT-51, no. 9, pp. 2029–2035, Sep. 2003.

[33] F. Bertazzi, O. A. Peverini, M. Goano, G. Ghione, R. Orta, and R. Tascone, "A fast reduced-order model for the full-wave FEM analysis of lossy inhomogeneous anisotropic waveguides," *IEEE Trans. Microw. Theory Techn.*, vol. MTT-50, no. 9, pp. 2108–2114, Sep. 2002.

[34] T. M. Inc., "MathWorks - Introduction to MATLAB," Natick, MA, USA, 2003, Accessed: Jan. 20, 2022. [Online]. Available: http://www.mathworks.com/products/matlab/

[35] S. Koeber *et al.*, "Femtojoule electro-optic modulation using a silicon-organic hybrid device," *Light Sci. Appl.*, vol. 4, Feb. 2015, Art. no. e255.

[36] D. A. B. Miller, "Energy consumption in optical modulators for interconnects," *Opt. Exp.*, vol. 20, no. S2, pp. A293–A308, 2012.